

# Efficient and stable noble-metal-free catalyst for acidic water oxidation

Sanjiang Pan<sup>1,2,3,4,5,14</sup>, Hao Li<sup>6,14</sup>, Dan Liu<sup>7</sup>, Rui Huang<sup>8</sup>, Xuelei Pan<sup>9</sup>, Dan Ren<sup>10</sup>, Jun Li<sup>10</sup>, Mohsen Shakouri<sup>11</sup>, Qixing Zhang<sup>1,2,3,4,5</sup>, Manjing Wang<sup>1,2,3,4,5</sup>, Changchun Wei<sup>1,2,3,4,5</sup>, Liqiang Mai<sup>12</sup>, Bo Zhang<sup>8</sup>, Ying Zhao<sup>1,2,3,4,5</sup>, Zhenbin Wang<sup>13</sup>✉, Michael Graetzel<sup>1,10</sup>✉ & Xiaodan Zhang<sup>1,2,3,4,5</sup>✉

Developing non-noble catalysts with superior activity and durability for oxygen evolution reaction (OER) in acidic media is paramount for hydrogen production from water. Still, challenges remain due to the inadequate activity and stability of the OER catalyst. Here, we report a cost-effective and stable manganese oxybromide ( $\text{Mn}_{7.5}\text{O}_{10}\text{Br}_3$ ) catalyst exhibiting an excellent OER activity in acidic electrolytes, with an overpotential of as low as  $295 \pm 5$  mV at a current density of  $10 \text{ mA cm}^{-2}$ .  $\text{Mn}_{7.5}\text{O}_{10}\text{Br}_3$  maintains good stability under operating conditions for at least 500 h. In situ Raman spectroscopy, X ray absorption near edge spectroscopy, and density functional theory calculations confirm that a self-oxidized surface with enhanced electronic transmission capacity forms on  $\text{Mn}_{7.5}\text{O}_{10}\text{Br}_3$  and is responsible for both the high catalytic activity and long-term stability during catalysis. The development of  $\text{Mn}_{7.5}\text{O}_{10}\text{Br}_3$  as an OER catalyst provides crucial insights into the design of non-noble metal electrocatalysts for water oxidation.

<sup>1</sup>Institute of Photoelectronic Thin Film Devices and Technology, Renewable Energy Conversion and Storage Center, Solar Energy Research Center, Nankai University, Tianjin 300350, PR China. <sup>2</sup>Key Laboratory of Photoelectronic Thin Film Devices and Technology of Tianjin, Tianjin 300350, PR China. <sup>3</sup>Haihe Laboratory of Sustainable Chemical Transformations, Tianjin 300192, PR China. <sup>4</sup>Engineering Research Center of Thin Film Photoelectronic Technology of Ministry of Education, Tianjin 300350, PR China. <sup>5</sup>Collaborative Innovation Center of Chemical Science and Engineering (Tianjin), Tianjin 300072, PR China. <sup>6</sup>Advanced Institute for Materials Research (WPI-AIMR), Tohoku University, Sendai 980-8577, Japan. <sup>7</sup>Institute of Flexible Electronics (IFE), Northwestern Polytechnical University (NPU), Xi'an 710072, PR China. <sup>8</sup>State Key Laboratory of Molecular Engineering of Polymers, Department of Macromolecular Science, Fudan University, Shanghai 200438, PR China. <sup>9</sup>State Key Laboratory of Advanced Technology for Materials Synthesis and Processing, International School of Materials Science and Engineering, Wuhan University of Technology, 430070 Wuhan, PR China. <sup>10</sup>Laboratory of Photonics and Interfaces, Ecole Polytechnique Federale de Lausanne, Lausanne 1015, Switzerland. <sup>11</sup>Canadian Light Source, Inc. (CLS), Saskatoon, Saskatchewan, Canada. <sup>12</sup>State Key Laboratory of Advanced Technology for Materials Synthesis and Processing, School of Materials Science and Engineering, Wuhan University of Technology, 430070 Wuhan, PR China. <sup>13</sup>Catalysis Theory Center, Department of Physics, Technical University of Denmark, Lyngby 2800, Denmark. <sup>14</sup>These authors contributed equally: Sanjiang Pan, Hao Li. ✉email: [zwang@fysik.dtu.dk](mailto:zwang@fysik.dtu.dk); [michael.graetzel@epfl.ch](mailto:michael.graetzel@epfl.ch); [xdzhang@nankai.edu.cn](mailto:xdzhang@nankai.edu.cn)

Proton exchange membrane (PEM) water electrolysis has the advantages of high current density, high gas purity, and rapid system response<sup>1–4</sup>. The acidic water electrolyzer of PEM is a promising technique to produce hydrogen on a large-scale<sup>5–7</sup>. However, the catalyst for the oxygen evolution reaction (OER) is prone to corrosion in an acidic environment, leading to severe instability. Only a few noble metal-based catalysts (e.g., IrO<sub>2</sub>) are resistant to corrosion and are currently being used in acidic water oxidation to obtain high activity and stability<sup>8–11</sup>. Extensive research efforts have been devoted to improving the performance of the noble-metal catalysts or developing noble-metal free catalysts to allow their widespread deployment<sup>12–16</sup>.

Over the past decades, the first-row transition metal-based compounds (e.g., Mn-, Co-, Ni-based oxides) have attracted considerable interest in searching for noble-metal-free materials as high-performance acidic OER electrocatalysts<sup>17–22</sup>. Nevertheless, the performance of these materials remains inferior to that of the noble metal-based catalysts, and most of them exhibit relatively high overpotentials, exceeding 370 mV at a current density of 10 mA/cm<sup>2</sup> or poor durability (<50 h) (Supplementary Table 1). The existence of a stable potential window under OER potentials in acidic media (Supplementary Fig. 1) makes Mn-based materials highly attractive as a basis for a stable and active catalyst for OER<sup>23,24</sup>. Many Mn-based oxides have been investigated by either doping with other elements<sup>17,25</sup> or optimizing morphologies<sup>26–28</sup> to improve their OER activity. Unfortunately, Mn-based materials considered so far commonly suffer from rather high overpotentials and poor electronic conductivity.

In this work, we introduce Mn<sub>7.5</sub>O<sub>10</sub>Br<sub>3</sub> as a low-cost and highly efficient OER catalyst in an acidic environment. The compound itself was first reported nearly 30 years ago<sup>29–31</sup>, but it has never been applied in electrocatalysis. We find that Mn<sub>7.5</sub>O<sub>10</sub>Br<sub>3</sub> exhibits an OER overpotential ( $\eta$ ) of 295 ± 5 mV at a current density of 10 mA/cm<sup>2</sup> and maintains good stability under operating conditions for at least 500 h. This performance is superior to the state-of-the-art noble-metal free catalyst<sup>23</sup> and comparable to that of noble-metal-containing catalysts, such as IrO<sub>x</sub> or SrIrO<sub>3</sub><sup>32</sup>. In-situ Raman spectroscopy combined with density functional theory (DFT) calculations were employed to investigate the catalytic activities and stabilities of different Mn-based materials ( $\gamma$ -MnO<sub>2</sub> and Mn-O-X, X = Cl, Br). Our experiments and calculations suggest that a close-packed oxide surface forms during OER due to a self-oxidation process, resulting in excellent long-term stability and an active phase for the OER reaction. In addition, the presence of halogen ions provides the catalyst with an enhanced electron transport capacity, further enhancing the OER activity.

## Results

**Materials characterization.** Mn<sub>8</sub>O<sub>10</sub>Cl<sub>3</sub>, Mn<sub>7.5</sub>O<sub>10</sub>Br<sub>3</sub>, and  $\gamma$ -MnO<sub>2</sub> were synthesized on carbon cloth through a solvothermal method. Supplementary Fig. 2 shows that the synthesized Mn<sub>7.5</sub>O<sub>10</sub>Br<sub>3</sub> is uniformly coated on the carbon cloth. Energy dispersive X-ray spectroscopy (EDS) confirms (Fig. 1a) that Mn, O, and Br elements are evenly distributed in the material with negligible impurity elements, confirming its high purity. These distinctive lattice fringes are assigned to the (213) and (303) crystal planes of Mn<sub>7.5</sub>O<sub>10</sub>Br<sub>3</sub> (Fig. 1b, c) with a lattice spacing of 0.305 and 0.258 nm, respectively, as determined from the high-resolution transmission electron microscopy (HRTEM). It should be mentioned that accurate determinations of catalyst surface under working conditions need operando characterizations. The phase structure of these catalysts was analyzed by X-ray diffraction (XRD) with the typical pattern presented in Fig. 1d, e. The Rietveld refinement analysis reveals that

Mn<sub>7.5</sub>O<sub>10</sub>Br<sub>3</sub> possesses a structure with lattice parameters of  $a = 9.3083 \text{ \AA}$  and  $c = 13.0561 \text{ \AA}$  and a space group of I4/mmm. On the other hand, the Mn<sub>8</sub>O<sub>10</sub>Cl<sub>3</sub> possesses a structure with lattice parameters of  $a = 9.3757 \text{ \AA}$  and  $c = 13.0369 \text{ \AA}$  and a space group of I4/mmm. The figures of merit of these refinements are  $R_p = 1.421\%$ ,  $R_{wp} = 1.928\%$  and  $\chi^2 = 5.677$  for Mn<sub>7.5</sub>O<sub>10</sub>Br<sub>3</sub> and  $R_p = 1.697\%$ ,  $R_{wp} = 2.327\%$  and  $\chi^2 = 8.445$  for Mn<sub>8</sub>O<sub>10</sub>Cl<sub>3</sub>. All these results indicate the successful synthesis of the target compounds.

**Evaluation of electrochemical activity.** The OER activities of Mn<sub>8</sub>O<sub>10</sub>Cl<sub>3</sub> and Mn<sub>7.5</sub>O<sub>10</sub>Br<sub>3</sub> catalysts were evaluated using linear sweep voltammetry at a scan rate of 1 mV s<sup>-1</sup> in 0.5 M sulfuric acid (pH = 0.3, Fig. 2a and Supplementary Fig. 3). The catalytic OER activity of  $\gamma$ -MnO<sub>2</sub> was also characterized for comparison. Among the three catalysts,  $\gamma$ -MnO<sub>2</sub> exhibits the highest overpotential of 413 ± 5 mV to reach the current density of 10 mA cm<sup>-2</sup>, which accords with previously reported results<sup>23</sup>. Mn<sub>8</sub>O<sub>10</sub>Cl<sub>3</sub> shows a better activity with an overpotential of 368 ± 5 mV while Mn<sub>7.5</sub>O<sub>10</sub>Br<sub>3</sub> has the lowest overpotential of 295 ± 5 mV, outperforming all previously reported noble-metal-free acidic OER electrocatalysts and even some noble metal-based electrocatalysts (Supplementary Table 1). A one-time-constant model, consisting of solution resistance in series ( $R_s$ ) with one parallel constant phase element-resistance (CPE- $R_{ct}$ ) element, fits the experimental data well at all the overpotentials tested (Fig. 2b). Electrochemical impedance spectroscopy (EIS) further indicates that Mn<sub>7.5</sub>O<sub>10</sub>Br<sub>3</sub> has the smallest charge transfer resistance ( $R_{ct}$ , 7.2  $\Omega$  in Fig. 2b). Thus, it is expected to yield the fastest electrode kinetics, compared to Mn<sub>8</sub>O<sub>10</sub>Cl<sub>3</sub> (12.4  $\Omega$ ) and  $\gamma$ -MnO<sub>2</sub> (26.8  $\Omega$ ), which is also confirmed by their DFT + U calculated band gaps, 0.18 eV for Mn<sub>7.5</sub>O<sub>10</sub>Br<sub>3</sub>, 0.46 eV for Mn<sub>8</sub>O<sub>10</sub>Cl<sub>3</sub>, and 0.53 eV for  $\gamma$ -MnO<sub>2</sub><sup>33</sup>. Due to the similar structural pattern (Supplementary Fig. 4), Mn<sub>7.5</sub>O<sub>10</sub>Br<sub>3</sub> and Mn<sub>8</sub>O<sub>10</sub>Cl<sub>3</sub> show somewhat comparable  $R_{ct}$ . Tafel slope analysis (Fig. 2c) also supports the enhanced OER catalytic activity of Mn<sub>7.5</sub>O<sub>10</sub>Br<sub>3</sub>. We derive a value of 68 mV dec<sup>-1</sup>, which is much smaller than the values of 90 mV dec<sup>-1</sup> and 91 mV dec<sup>-1</sup> derived for  $\gamma$ -MnO<sub>2</sub> and Mn<sub>8</sub>O<sub>10</sub>Cl<sub>3</sub>, respectively. The exchange current density ( $I_{ex}$ ), a key parameter to judge catalytic activity, can be estimated from the intercept of a linear Tafel plot. The  $I_{ex}$  values for Mn<sub>7.5</sub>O<sub>10</sub>Br<sub>3</sub>, Mn<sub>8</sub>O<sub>10</sub>Cl<sub>3</sub>, and  $\gamma$ -MnO<sub>2</sub> are  $1.1 \times 10^{-4}$ ,  $7.7 \times 10^{-5}$ , and  $1.5 \times 10^{-5}$  mA cm<sup>-2</sup>, respectively. The Mn<sub>7.5</sub>O<sub>10</sub>Br<sub>3</sub> catalyst gives a larger  $I_{ex}$  than Mn<sub>8</sub>O<sub>10</sub>Cl<sub>3</sub> and  $\gamma$ -MnO<sub>2</sub>, suggesting the fastest electrode kinetics and is on the same order of magnitude as commercial RuO<sub>2</sub> ( $3.415 \times 10^{-4}$  mA cm<sup>-2</sup>)<sup>34</sup>. Interestingly, Mn<sub>7.5</sub>O<sub>10</sub>Br<sub>3</sub> is found to have a smaller double-layer capacitance of 248.2 mF cm<sup>-2</sup> ( $C_{dl}$ ) compared to Mn<sub>8</sub>O<sub>10</sub>Cl<sub>3</sub> (332.9 mF cm<sup>-2</sup>) and  $\gamma$ -MnO<sub>2</sub> (320.6 mF cm<sup>-2</sup>), as shown in Supplementary Fig. 5. Though Mn<sub>8</sub>O<sub>10</sub>Cl<sub>3</sub> offers the highest density of exposed active sites per geometric electrode area, its performance is relatively inferior to that of Mn<sub>7.5</sub>O<sub>10</sub>Br<sub>3</sub> even though the latter exposes a lower level of active sites.

We further calculated specific mass activities of the as-prepared catalysts at a set potential of 1.65 V (vs. RHE). Mn<sub>7.5</sub>O<sub>10</sub>Br<sub>3</sub> displays the highest geometric current density of 147.77 mA cm<sup>-2</sup> with a mass activity of 20.57 A g<sup>-1</sup>, compared with Mn<sub>8</sub>O<sub>10</sub>Cl<sub>3</sub> (32.76 mA cm<sup>-2</sup>, 4.66 A g<sup>-1</sup>) and  $\gamma$ -MnO<sub>2</sub> (12.51 mA cm<sup>-2</sup>, 2.05 A g<sup>-1</sup>). These data demonstrate the enhanced catalytic activity of Mn<sub>7.5</sub>O<sub>10</sub>Br<sub>3</sub>, which is more than four times higher than that of Mn<sub>8</sub>O<sub>10</sub>Cl<sub>3</sub> and ten times that of  $\gamma$ -MnO<sub>2</sub>. The turnover frequency (TOF) is the most suitable metric to compare the OER activity<sup>35–38</sup>. The TOF was calculated based on assuming a 100% dispersion of the catalysts. From our analysis, the Mn<sub>7.5</sub>O<sub>10</sub>Br<sub>3</sub> catalyst exhibits the highest TOF of  $3.3 \times 10^{-3}$  s<sup>-1</sup>, exceeding that of Mn<sub>8</sub>O<sub>10</sub>Cl<sub>3</sub> ( $4.5 \times 10^{-4}$  s<sup>-1</sup>) and  $\gamma$ -MnO<sub>2</sub> ( $1.4 \times 10^{-5}$  s<sup>-1</sup>), (Fig. 2d).

The stability of these three OER catalysts was investigated by chronopotentiometry at 10 mA cm<sup>-2</sup>. Noteworthy, Mn<sub>7.5</sub>O<sub>10</sub>Br<sub>3</sub>

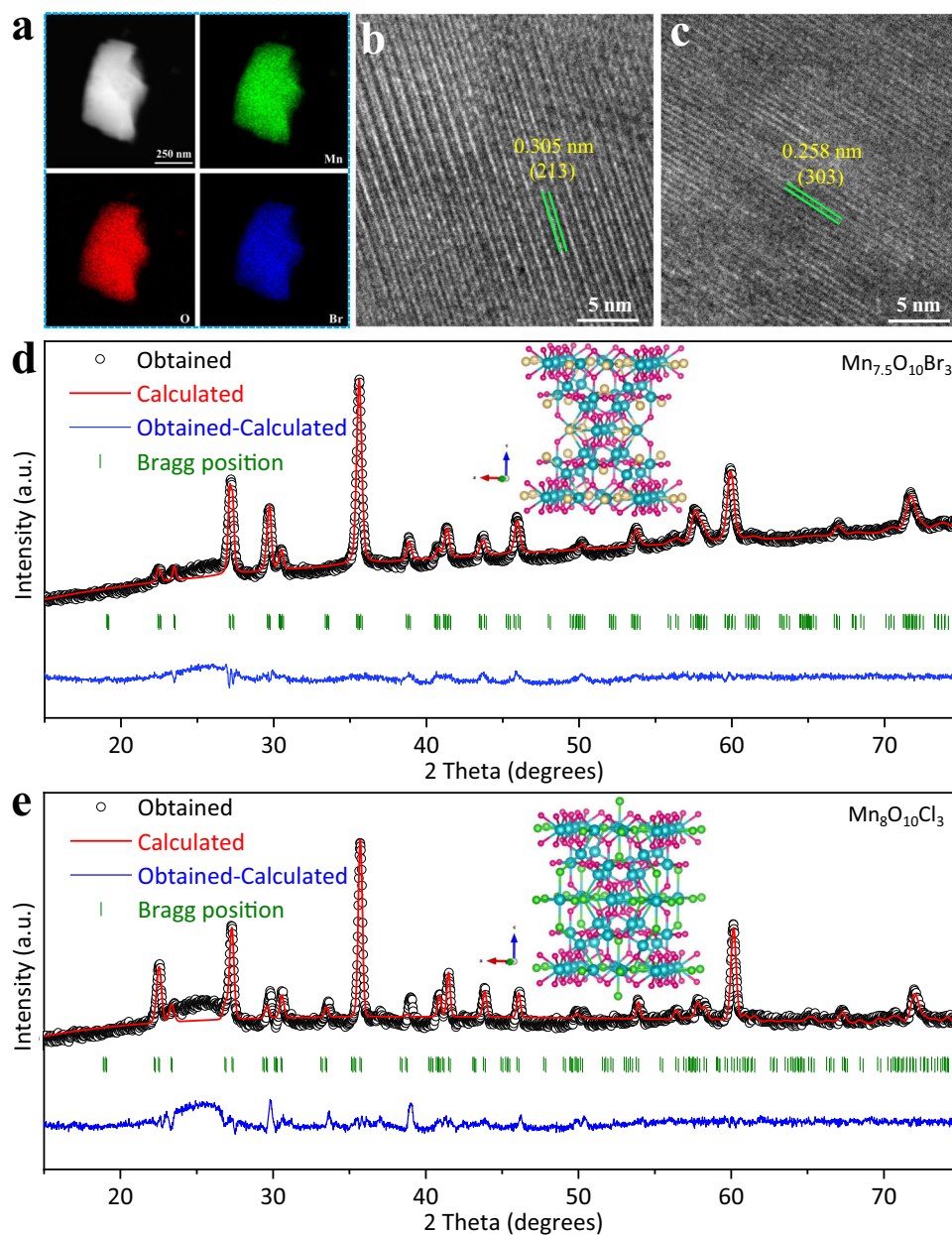


**Fig. 1** Structural characterization of  $\text{Mn}_{7.5}\text{O}_{10}\text{Br}_3$ . **a** HAADF-STEM image and EDS mapping images; HRTEM image of the surface **b** (213) and **c** (303); **d** Refined X-ray diffraction (XRD) patterns of  $\text{Mn}_{7.5}\text{O}_{10}\text{Br}_3$ , **e** Refined XRD patterns of  $\text{Mn}_8\text{O}_{10}\text{Cl}_3$ .

exhibits excellent stability, showing a rate of the potential increase of only 0.088 mV/h to maintain the current during 500 h of operation on FTO (Fig. 2e). This is comparable to other non-noble metal catalysts (See Supplementary Table 1 and the discussion there). In particular, compared to the stability of  $\text{IrO}_x/\text{SrIrO}_3$  where no potential increase was observed within 30 h<sup>32</sup>, the potential of our  $\text{Mn}_{7.5}\text{O}_{10}\text{Br}_3$  merely increases by 15.6 mV over the same period. Regarding the durability of  $\text{Mn}_8\text{O}_{10}\text{Cl}_3$ , we observed a sharp voltage rise after 75 h (Supplementary Fig. 6), suggesting it to be poorer than that of  $\text{Mn}_{7.5}\text{O}_{10}\text{Br}_3$ . This is likely because the operating potential of  $\text{Mn}_8\text{O}_{10}\text{Cl}_3$  at 10 mA cm<sup>-2</sup> is relatively higher and slightly beyond the electrochemical stability window, leading to the corrosion of the catalyst. The X-ray diffractograms of  $\text{Mn}_{7.5}\text{O}_{10}\text{Br}_3$  measured before and after the stability test show more intense characteristic peaks of the catalyst  $\text{Mn}_{7.5}\text{O}_{10}\text{Br}_3$ . We suspect that those above changes may be caused by the

detachment of a small amount of the catalysts from the FTO after a long period of stability (Supplementary Fig. 7), and this could be the reason for the potential increase of about 44 mV with an increased rate of 0.088 mV/h. At the same time, we find that the FTO substrate could better showcase the stability of the catalyst than carbon cloth when conducting long-term stability tests under OER working conditions (Supplementary Fig. 8). Overall, the structure of  $\text{Mn}_{7.5}\text{O}_{10}\text{Br}_3$  is preserved during long-term operation. The HRTEM after stability measurement further confirms the high stability of the catalyst (Supplementary Fig. 9). Besides, the chemical composition of the catalyst and the bonding environment of the metal center was also examined by EDS mapping and X-ray photoelectron spectroscopy (XPS) (Supplementary Figs. 10, 11). High-resolution XPS spectra of Mn 2p of electrolyte before and after stability test confirm that Mn remains inside the lattice (Supplementary Fig. 12) without any obvious dissolution for 500 h, during which the catalyst attained a number

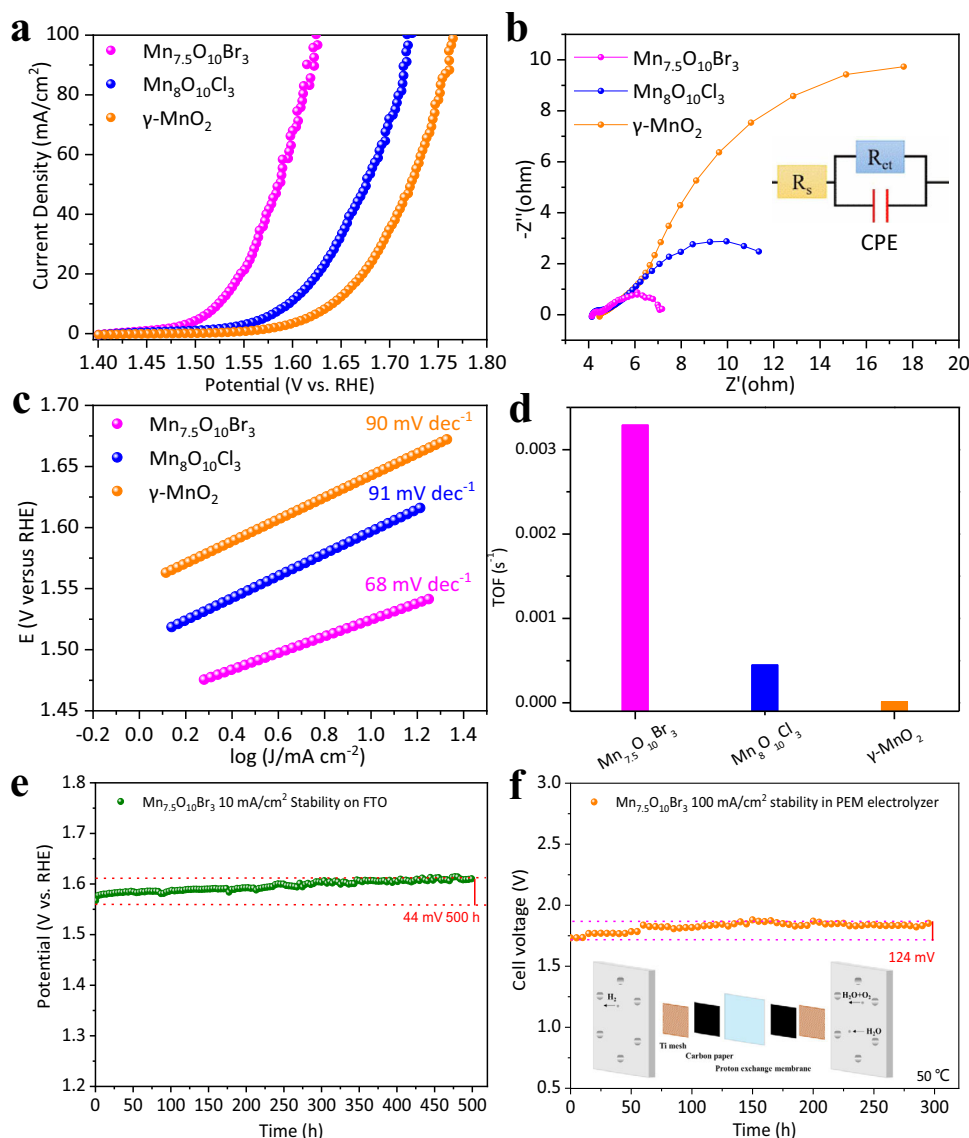


**Fig. 2** Evaluation of OER electrochemical activity. **a** LSV curves of different catalysts at 1 mV/s scan rate with iR correction. **b** Electrochemical impedance spectra (EIS) at 1.40 V (set potential). The equivalent circuit is shown ( $R_s$ : series resistance;  $R_{ct}$ : charge-transfer resistance). **c** Tafel plots of  $Mn_{7.5}O_{10}Br_3$ ,  $Mn_8O_{10}Cl_3$ , and  $\gamma$ - $MnO_2$ . **d** TOF calculated from the current density at an iR-corrected overpotential of 300 mV. **e** Chronopotentiometry curves (On FTO) of  $Mn_{7.5}O_{10}Br_3$  at 10 mA  $cm^{-2}$  (25 °C). **f** Chronopotentiometry tests of the  $Mn_{7.5}O_{10}Br_3$  oxide catalyst at 100 mA  $cm^{-2}$  in the PEM electrolyzer measured at 50 °C. Inset photo: PEM electrolyzer architecture. Source data are provided as a Source Data file.

of  $5.3 \times 10^3$  turnovers. Moreover, the Inductively Coupled Plasma Optical Emission Spectrometry (ICP-OES) results show dissolved manganese of  $Mn_{7.5}O_{10}Br_3$  (1.05 ppm) is nearly 9 $\times$  lower than that of  $Mn_8O_{10}Cl_3$  (8.74 ppm) and 7 $\times$  lower than that of  $\gamma$ - $MnO_2$  (6.86 ppm) (Supplementary Table 2), suggesting better stability of  $Mn_{7.5}O_{10}Br_3$ . Meanwhile, no Mn ions were deposited on the counter electrode as shown by Inductively Coupled Plasma Mass Spectrometry (ICP-MS). The Faradaic efficiency for  $O_2$  production on three catalysts was quantified by online gas chromatography (Supplementary Fig. 13). All three samples showed high values of faradaic efficiency for oxygen evolution, namely,  $99.1\% \pm 2.2\%$  on  $Mn_{7.5}O_{10}Br_3$ ,  $96.2\% \pm 7.1\%$  on  $Mn_8O_{10}Cl_3$ , and  $96.3\% \pm 1.0\%$  on  $\gamma$ - $MnO_2$  (Supplementary Figs. 14–16). The slightly smaller values for  $Mn_8O_{10}Cl_3$  and  $\gamma$ - $MnO_2$  compared to  $Mn_{7.5}O_{10}Br_3$  may be due to some side reactions such as corrosion. To further evaluate the performance of  $Mn_{7.5}O_{10}Br_3$  in industrial operating systems, we next used the catalyst in a PEM electrolyzer at 50 °C (Supplementary Fig. 17). Upon applying a constant

current of 100 mA  $cm^{-2}$ , a cell voltage increase of 124 mV was observed during 300 h of electrolysis (Fig. 2f). Compared to  $\gamma$ - $MnO_2$ , which becomes inactivated after 12 h operation at 100 mA  $cm^{-2}$  in a PEM electrolyzer at 25 °C<sup>23</sup>,  $Mn_{7.5}O_{10}Br_3$  exhibits considerably superior stability at 50 °C, rendering it attractive as a noble-metal-free OER catalyst with excellent activity and stability in acidic media.

**XPS, X-ray absorption near-edge spectroscopy, and in-situ Raman analysis for mechanistic investigations.** Mn 3s exchange splitting  $\Delta E_{3s}$  (Eq. 1) is well established to be linearly correlated with the average valence state of manganese ( $V_{Mn}$ )<sup>39,40</sup>, and thus can be used to determine the Mn valence state.  $V_{Mn}$  is determined to be 3.130 for  $Mn_{7.5}O_{10}Br_3$  and 2.939 for  $Mn_8O_{10}Cl_3$  based on the corresponding  $\Delta E_{3s}$  values of 5.15 eV and 5.30 eV (Fig. 3a and Supplementary Fig. 18).  $V_{Mn}$  (3.137) in  $Mn_{7.5}O_{10}Br_3$  changes negligibly after longtime operations, suggesting excellent catalyst stability (Supplementary Fig. 19). Moreover, deconvolution of the



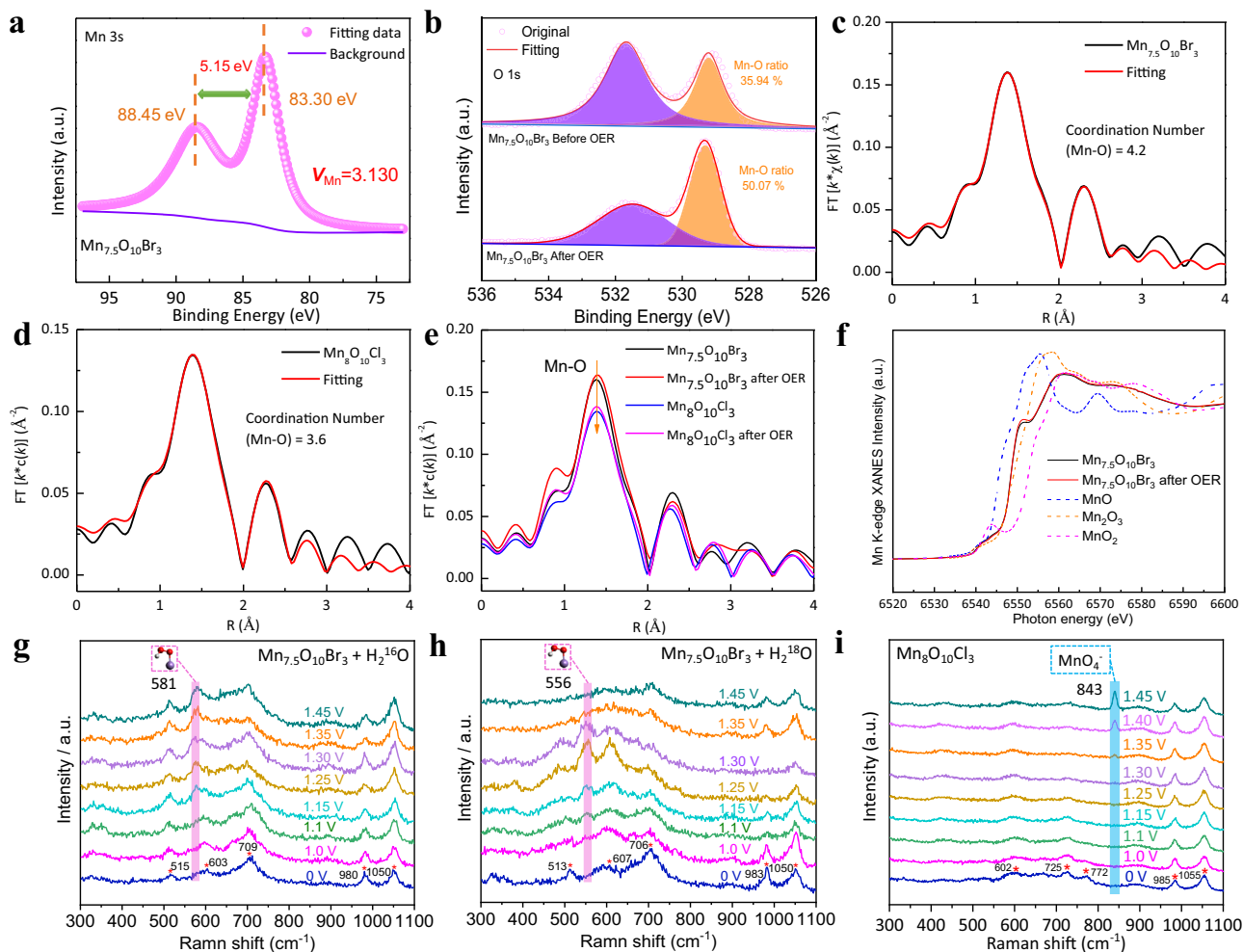


**Fig. 3 Electronic structure characterization and mechanistic investigations.** High-resolution XPS spectra of  $\text{Mn}_{7.5}\text{O}_{10}\text{Br}_3$  **a** Mn 3s and **b** O 1s; EXAFS spectra of the  $\text{Mn}_{7.5}\text{O}_{10}\text{Br}_3$  (**c**),  $\text{Mn}_8\text{O}_{10}\text{Cl}_3$  (**d**) and compared with  $\text{Mn}_{7.5}\text{O}_{10}\text{Br}_3$  and  $\text{Mn}_8\text{O}_{10}\text{Cl}_3$  after OER stability (**e**); Normalized Mn K-edge XANES spectra of  $\text{Mn}_{7.5}\text{O}_{10}\text{Br}_3$ ,  $\text{Mn}_{7.5}\text{O}_{10}\text{Br}_3$  after the stability and reference materials (**f**); In-situ Raman spectra of  $\text{Mn}_{7.5}\text{O}_{10}\text{Br}_3$  catalyst on a carbon cloth in 0.5 M  $\text{H}_2\text{SO}_4 + \text{H}_2^{16}\text{O}$  (**g**) and 0.5 M  $\text{H}_2\text{SO}_4 + \text{H}_2^{18}\text{O}$  (**h**) electrolyte under different external applied potential (0–1.45 V); In-situ Raman spectra of  $\text{Mn}_8\text{O}_{10}\text{Cl}_3$  catalyst on a carbon cloth in 0.5 M  $\text{H}_2\text{SO}_4 + \text{H}_2^{16}\text{O}$  (**i**) electrolyte under different external applied potential (0–1.45 V).

high-resolution XPS spectra of O 1s (Fig. 3b) reveals that the integral area of Mn-O area increased from 35.94% to 50.07%, compared with smaller augmentation for  $\text{Mn}_8\text{O}_{10}\text{Cl}_3$  (46.49–53.83%) and  $\gamma\text{-MnO}_2$  (46.77–47.97%). Thus,  $\text{Mn}_{7.5}\text{O}_{10}\text{Br}_3$  experiences the largest electro-oxidation under OER conditions (Supplementary Figs. 20, 21, and Table 3). Our DFT-calculated surface Pourbaix diagrams, discussed below, will further interpret this electro-oxidation process. To precisely analyze the valence state and the formation of close-packed oxide surface, X-ray absorption near-edge spectroscopy (XANES) and extended X-ray absorption fine structure (EXAFS) with Fourier transform was applied to characterize  $\text{Mn}_{7.5}\text{O}_{10}\text{Br}_3$  and  $\text{Mn}_8\text{O}_{10}\text{Cl}_3$ . MnO,  $\text{Mn}_2\text{O}_3$ , and  $\text{MnO}_2$  were employed as reference materials. The Mn K-edge absorption onsets of  $\text{Mn}_8\text{O}_{10}\text{Cl}_3$  and  $\text{Mn}_{7.5}\text{O}_{10}\text{Br}_3$  are close to that of  $\text{Mn}_2\text{O}_3$  ( $\text{Mn}^{3+}$ ).  $\text{Mn}_{7.5}\text{O}_{10}\text{Br}_3$  shows a more positive absorption onset than  $\text{Mn}_8\text{O}_{10}\text{Cl}_3$ , indicating that the Mn species in  $\text{Mn}_{7.5}\text{O}_{10}\text{Br}_3$  have a higher valence state than those in  $\text{Mn}_8\text{O}_{10}\text{Cl}_3$ , consistent with XPS results (Supplementary Fig. 22). The increase of Mn valence state from  $\text{Mn}_8\text{O}_{10}\text{Cl}_3$  to  $\text{Mn}_{7.5}\text{O}_{10}\text{Br}_3$  aligns well with the increase of Mn-O coordination from 3.6 in  $\text{Mn}_8\text{O}_{10}\text{Cl}_3$  to 4.2 in  $\text{Mn}_{7.5}\text{O}_{10}\text{Br}_3$ , as revealed by EXAFS fittings (Fig. 3c, d). The slight increase of Mn-O coordination in  $\text{Mn}_8\text{O}_{10}\text{Cl}_3$  and  $\text{Mn}_{7.5}\text{O}_{10}\text{Br}_3$  after OER further suggests the

formation of the close-packed oxide surface of these materials (Fig. 3e). The Mn valence state shows almost no change before and after OER, indicating excellent stability of these materials (Fig. 3f and Supplementary Fig. 23). Collectively, these results give clear evidence of the formation of a close-packed oxide surface and excellent structural stability of  $\text{Mn}_{7.5}\text{O}_{10}\text{Br}_3$  in acid media.

To gain deeper insight into the OER reaction mechanism, in-situ Raman spectroscopy was utilized to better understand the active interfacial phase of the catalyst during the electrochemical process. Under acidic conditions, the OER process generally proceeds via a four-electron transfer process, i.e., water is successively oxidized to form Mn-OH, Mn-O, and Mn-OOH species, and finally, produce oxygen. Figure 3g–i, and Supplementary Fig. 24 show a series of Raman spectra for the three catalysts immersed in 0.5 M  $\text{H}_2\text{SO}_4$  at selected applied potentials vs. the Ag/AgCl electrode (saturated KCl). We assign the peaks at 515, 603 and 709  $\text{cm}^{-1}$  to Mn-O stretch vibrations<sup>41</sup> of  $\text{Mn}_{7.5}\text{O}_{10}\text{Br}_3$  and peaks at 980 and 1050  $\text{cm}^{-1}$  from  $\text{SO}_4^{2-}$ . Because of the chemical environment changes of Mn-O bond in  $\text{Mn}_8\text{O}_{10}\text{Cl}_3$ <sup>42,43</sup>, we assign the peaks at 602, 725, and 772  $\text{cm}^{-1}$  to Mn-O stretch vibrations for  $\text{Mn}_8\text{O}_{10}\text{Cl}_3$  and the peaks at 985 and 1055  $\text{cm}^{-1}$  to  $\text{SO}_4^{2-}$ .  $\text{Mn}_{7.5}\text{O}_{10}\text{Br}_3$  catalyst displays a distinct

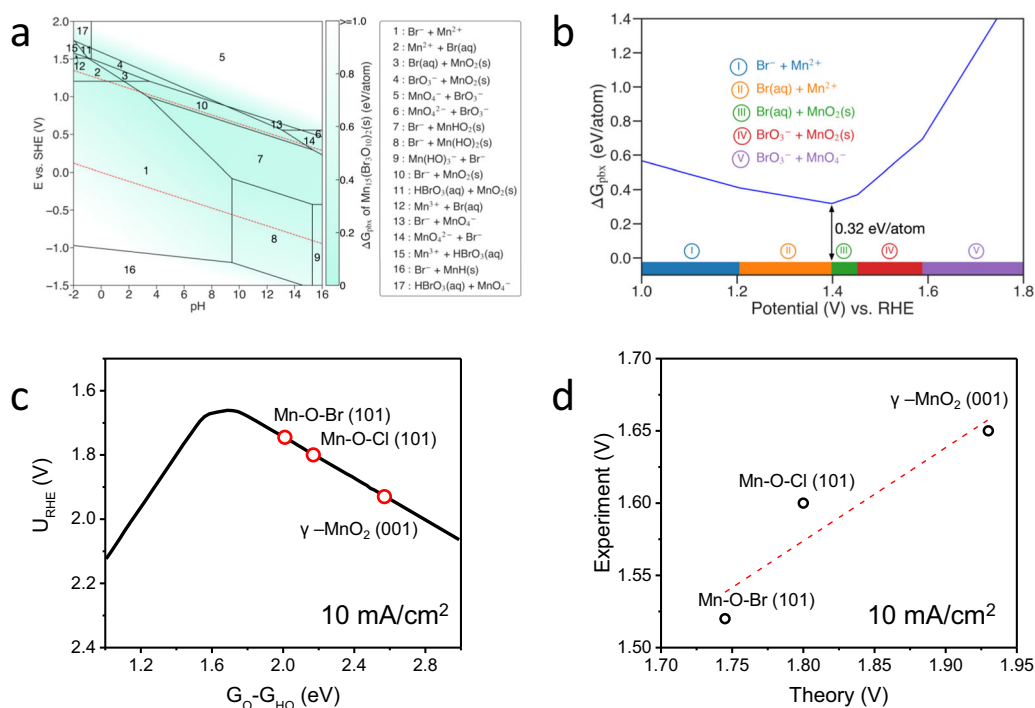


**Fig. 4 Theoretical analysis of OER stability and activity.** **a** Calculated Mn-O-Br Pourbaix diagrams generated with aqueous ions concentration of  $10^{-4}$  M at 25 °C. The Mn ions concentration used is based on the ICP-OES measurement. The Lake blue color measures the stability of  $\text{Mn}_{7.5}\text{O}_{10}\text{Br}_3$  at relevant potential and pH. The water stability window is shown in a red dashed line. **b** Calculated Pourbaix decomposition free energy ( $\Delta G_{\text{pbx}}$ ) of  $\text{Mn}_{7.5}\text{O}_{10}\text{Br}_3$  from the potential 1.0–1.8 V vs. RHE at pH = 0. The projection of  $\Delta G_{\text{pbx}}$  onto the potential axis shows the stable species at the corresponding regions. **c** Kinetic OER activity volcano plot at  $10 \text{ mA/cm}^2$  as a function of  $G_{\text{O}}-G_{\text{H}_2\text{O}}$ . **d** Theory-predicted OER potentials vs. experimental values at  $10 \text{ mA/cm}^2$ .

Raman peak at  $581 \text{ cm}^{-1}$ , whose intensity increases along with sweeping potential (Fig. 3g). The Raman peaks observed at  $581 \text{ cm}^{-1}$  can well be assigned to the Mn-OOH species<sup>44–46</sup>. When comparing the Raman spectra measured in  $\text{H}_2^{16}\text{O}$  and  $\text{H}_2^{18}\text{O}$  electrolyte at 1.25 V (OER onset potential), we observe a ca.  $26 \text{ cm}^{-1}$  negative shift in  $\text{Mn}_{7.5}\text{O}_{10}\text{Br}_3$  (Fig. 3h and Supplementary Fig. 25), indicating that the Mn- $^{18}\text{O}^{18}\text{OH}$  adsorbed species is formed by the isotope exchange of the two  $^{16}\text{O}$  atoms (Eq. 7). According to Eq. (16), its characteristic peak will be at  $556 \text{ cm}^{-1}$ . Further Raman test under constant voltage revealed that the Raman peak area around  $581 \text{ cm}^{-1}$  was directly proportional to the current density, and would become weaker with the decrease of the current density (Supplementary Fig. 26). Therefore, we can rule out the possibility of interference caused by by-products. Differently, the Raman peak at  $843 \text{ cm}^{-1}$  is assigned to the  $\text{MnO}_4^-$  species<sup>47,48</sup>, which gradually appears on the  $\text{Mn}_8\text{O}_{10}\text{Cl}_3$  and  $\gamma\text{-MnO}_2$  surface under positive potential sweeping (Fig. 3i and Supplementary Fig. 24). This band intensity also increases upon augmenting the applied potential, clearly suggesting an accumulation of  $\text{MnO}_4^-$  oxidative product on the  $\text{Mn}_8\text{O}_{10}\text{Cl}_3$  and  $\gamma\text{-MnO}_2$  surfaces. These results show that  $\text{HOO}^*$  is the dominant species on the  $\text{Mn}_{7.5}\text{O}_{10}\text{Br}_3$  surface, and  $\text{Mn}_{7.5}\text{O}_{10}\text{Br}_3$  possesses better stability than  $\text{Mn}_8\text{O}_{10}\text{Cl}_3$  and  $\gamma\text{-MnO}_2$ .

**Theoretical analysis.** To further understand the stability and activity of the catalysts, DFT calculations were performed to calculate the aqueous decomposition free energy<sup>49</sup> and theoretical OER limiting potentials using the recently developed microkinetic OER model<sup>50</sup>. The aqueous decomposition free energy ( $\Delta G_{\text{pbx}}$ ), obtained based on the DFT-calculated bulk Pourbaix diagram (Fig. 4a and Supplementary Fig. 27a), measures the catalyst stability at ambient pH and electrode potential. The calculated

$\Delta G_{\text{pbx}}$  shows that  $\text{Mn}_{7.5}\text{O}_{10}\text{Br}_3$  and  $\text{Mn}_8\text{O}_{10}\text{Cl}_3$  can be stabilized by forming a  $\text{MnO}_x$  (e.g.,  $\text{MnO}_2$ ) passivation layer on the surface at the potential of 1.40–1.60 V vs. RHE at pH = 0 (Fig. 4b and Supplementary Fig. 27b). Compared to  $\text{Mn}_{7.5}\text{O}_{10}\text{Br}_3$ , the higher operating potential of  $\text{Mn}_8\text{O}_{10}\text{Cl}_3$  makes it suffer from a larger thermodynamic driving force to decompose, which explains our experimental observations that Mn-O-Br exhibits better stability than Mn-O-Cl at operating conditions. Figure 4c shows the derived microkinetic volcano model at  $10 \text{ mA/cm}^2$  as the function of  $G_{\text{O}}-G_{\text{H}_2\text{O}}$ . This microkinetic model was derived by estimating the kinetics and thermodynamics of each elementary step based on the previously discovered linear scaling relations on transition metal oxides as a function of  $G_{\text{H}_2\text{O}}$  (e.g.,  $G_{\text{H}_2\text{O}}$  vs.  $G_{\text{O}}$ ,  $G_{\text{H}_2\text{O}}$  vs.  $G_{\text{HOO}}$ , and  $G_{\text{H}_2\text{O}}$  vs. transition state energies). The potential-dependent transition state energies were calculated based on the climbing image nudged elastic band (NEB) method<sup>51</sup> with explicit solvation models over different transition metal oxide surfaces using charge-extrapolation<sup>50</sup>. The completed modeling method, scaling relations, and details of this model are shown in Ref. 50. The theoretical activities of the three catalysts were analyzed by identifying the favorable surfaces, favorable surface states under operating potentials (based on surface Pourbaix diagram analysis), and active sites, with all details described in the Supplementary Discussion and Supplementary Figs. 28–31. Our surface Pourbaix diagram analyses clearly indicate that the  $\text{Mn}_{7.5}\text{O}_{10}\text{Br}_3$  and  $\text{Mn}_8\text{O}_{10}\text{Cl}_3$  (101) surfaces undergo a significant electro-oxidation process at the operating acidic OER conditions (Supplementary Figs. 29, 30), in excellent agreement with experiments shown in Supplementary Figs. 20, 21, and Table 3. By identifying the most favorable adsorption site (i.e., the site with the strongest HO-bonding at the surface identified by the surface Pourbaix diagram calculations in Supplementary Figs. 28–30), our kinetic volcano model allows predicting the OER potential as the function of the current density

and the calculated  $G_{\text{O}}-G_{\text{HO}}$  value (Fig. 4c). Our results show that the order of OER activity is  $\text{Mn-O-Br} > \text{Mn-O-Cl} > \gamma\text{-MnO}_2$ . Plotting the theory-predicted OER potential vs. the experimental potential at  $10 \text{ mA/cm}^2$  (Fig. 4d and Supplementary Table 4), a qualitative agreement was obtained with a constant deviation of  $\sim 0.2 \text{ V}$  on Mn-O-Br and Mn-O-Cl. This constant shifting may originate from the systematic DFT errors<sup>52</sup> or the roughness of the oxide surfaces under experimental conditions. It should be noted that the formation of a more close-packed oxide surface during operating conditions will lead to an active phase of the catalyst with a weakened OER adsorbate bound with lower adsorbate-metal coordination (Supplementary Fig. 31). This suggests that the formed  $\text{MnO}_x$  layer not only improves the catalysts' long-term stability but also promotes the catalytic activity, in good agreement with our experimental observations (Fig. 3).

**Outlook.** We note that the  $\text{Mn}_{7.5}\text{O}_{10}\text{Br}_3$  catalyst will have a  $124 \text{ mV}$  overpotential increase after  $300 \text{ h}$  operation in the PEM electrolytic cell, which is better than most non-noble metal catalysts (Supplementary Table 1) but is less stable than iridium oxide. It should be also mentioned that the catalyst may become inactivated under certain extreme conditions, such as large current density (e.g.,  $1 \text{ A cm}^{-2}$ ) and long-term operation (e.g.,  $>10 \text{ kh}$ ). Researchers still need to continue the search for new materials or optimize existing structures to achieve catalytic performance comparable to or better than noble metal catalysts. Given the high cost of noble metals, especially Ir, there is also a need to evaluate the cost-effectiveness of non-precious and precious OER catalysts in the future. Notably, according to our findings, the Mn-halogen interaction and the formation of a close-packed oxide surface are key factors in improving catalytic activity and stability, which provide effective guidance for further developing non-noble metal catalysts with excellent performance.

## Discussion

In summary, we have explored the potential of manganese oxyhalides ( $\text{MnXO}$ ;  $\text{X} = \text{Cl}, \text{Br}$ ) as acidic oxygen evolution reaction catalysts. In particular,  $\text{Mn}_{7.5}\text{O}_{10}\text{Br}_3$  achieved superior performance in acid solution with a low overpotential of  $295 \pm 5 \text{ mV}$  at a current density of  $10 \text{ mA cm}^{-2}$  and long-term stability of  $500 \text{ h}$ . XPS, XANES, and DFT results show that self-oxidation occurs on the surface of the material under OER operating conditions, consistent with the formation of a close-packed oxide surface and lower overpotentials. Our DFT calculations further show the formed close-packed oxide surface optimizes binding energies of the OER intermediate adsorbate. The Mn-halogen interaction could be the critical factor in improving the electron transport capacity.  $\text{Mn}_{7.5}\text{O}_{10}\text{Br}_3$ , therefore, may serve as a viable alternative to replacing noble-metal OER catalysts. The unique structure and formation of a close-packed oxide surface, strongly related to a high OER activity and stability, would provide valuable insights for designing more effective and stable electrochemical catalysts.

## Methods

**Chemicals.**  $\text{Mn}(\text{NO}_3)_2 \cdot 4\text{H}_2\text{O}$  (99.99%, AR, grade) was purchased from Innochem,  $\text{MnBr}_2 \cdot 4\text{H}_2\text{O}$  was purchased from Energy Chemical (99.9% AR, grade),  $\text{MnCl}_2 \cdot 4\text{H}_2\text{O}$  was purchased from Macklin (99.9% AR, grade), Carbon cloth substrates were purchased from CeTech (Taiwan). All chemicals were used without further purification.

**Synthesis of  $\text{Mn}_{7.5}\text{O}_{10}\text{Br}_3$ .** First,  $143.4 \text{ mg}$   $\text{MnBr}_2 \cdot 4\text{H}_2\text{O}$  was added in  $300 \mu\text{L}$   $\text{H}_2\text{O}$ , and then treated with ultrasound until dissolved. The obtained solution was mixed in  $500 \mu\text{L}$   $4 \text{ M Mn}(\text{NO}_3)_2 \cdot 4\text{H}_2\text{O}$  solution. We transferred a volume of  $300 \mu\text{L}$  of the above mixture into  $1 \text{ mL}$  centrifuge tube. Then, a  $2.5 \times 2.5 \text{ cm}^2$  hydrophilic carbon cloth was placed on a hotplate,  $300 \mu\text{L}$  of the above mixture was dropped on it, followed by calcination on a hotplate at  $250^\circ\text{C}$  in the air for  $5 \text{ h}$ . After cooling to room temperature, the resultant electrode was rinsed with Milli-Q ultra-pure water

and sonicated for  $30 \text{ s}$ . Finally, the electrodes were dried in an oven at  $65^\circ\text{C}$  overnight before being used.

**Synthesis of  $\text{Mn}_3\text{O}_{10}\text{Cl}_3$  and  $\gamma\text{-MnO}_2$ .** First,  $92.4 \text{ mg}$   $\text{MnCl}_2 \cdot 4\text{H}_2\text{O}$  was added in  $300 \mu\text{L}$   $\text{H}_2\text{O}$ , and then treated with ultrasonic until dissolved. The obtained solution was mixed in  $500 \mu\text{L}$   $4 \text{ M Mn}(\text{NO}_3)_2 \cdot 4\text{H}_2\text{O}$  solution. We transferred a volume of  $300 \mu\text{L}$  of the above mixture into  $1 \text{ mL}$  centrifuge tube. Then, a  $2.5 \times 2.5 \text{ cm}^2$  hydrophilic carbon cloth was placed on a hotplate,  $300 \mu\text{L}$  of the above mixture was dropped on it, followed by calcination on a hotplate at  $250^\circ\text{C}$  in the air for  $5 \text{ h}$ . After cooling to room temperature, the resultant electrode was rinsed with Milli-Q ultra-pure water and sonicated for  $30 \text{ s}$ . Finally, the electrodes were dried in an oven at  $65^\circ\text{C}$  overnight before being used.

The  $\gamma\text{-MnO}_2$  catalyst was synthesized following a process similar to that of the  $\text{Mn}_3\text{O}_{10}\text{Cl}_3$  catalyst, without the addition of the  $\text{MnCl}_2 \cdot 4\text{H}_2\text{O}$  precursors.

**Characterization.** The phase composition of the samples was characterized by the XRD (PAN analytical X'Pert Pro Diffractometer with operating parameters of Cu K $\alpha$  radiation ( $\lambda = 1.5418 \text{ \AA}$ ) at  $10\text{--}80^\circ(2\theta)$  at  $40 \text{ kV}$  voltage and  $40 \text{ mA}$  current) and the XPS with ESCALab220i-XL electron spectrometer. The morphology and composition of the samples were determined by FESEM under Hitachi S-4800 microscope with an acceleration voltage of  $20.0 \text{ kV}$  and TEM with a JEOLJEM-2010 instrument operating at  $200 \text{ kV}$ . Structure refinements of the XRD patterns were carried out using Rietica 1.7.7 software. In the refining process, the scale factor, background parameters, counter zero, and other general parameters are optimized. The space group of the catalyst was preliminarily determined by Le Bail thinning method, and the lattice parameters of the catalyst were approximately calculated. X-ray absorption spectra at the Mn K-edge were performed at the Soft X-ray Microcharacterization Beamline of the Canadian Light Source (CLS, Saskatoon, Saskatchewan, Canada). During measurements, X-ray beams with an incidence angle of  $45^\circ$  were used, and fluorescence yield was collected using silicon drift detectors. XANES and EXAFS spectra were analyzed using the Athena and Artemis softwares, respectively, included in a standardized IFFFIT package.<sup>53</sup> The manganese content of electrolyte was determined using ICP-OES (ICAP 7400) and ICP-MS (Elan drc-e). Raman spectroscopy (RTS-HiR-AM) at  $532 \text{ nm}$  excitation wavelength was used. In situ Raman (Supplementary Fig. 26) was normalized with the integral area of the characteristic peak of  $\text{SO}_4^{2-}$  around  $1052 \text{ cm}^{-1}$ , and then we performed peak fitting to divide the characteristic peak into two peaks around  $581 \text{ cm}^{-1}$  and  $603 \text{ cm}^{-1}$ , and then processed the Raman peak around  $581 \text{ cm}^{-1}$  corresponding to  $1.45 \text{ V}$ . All fitting standard deviations ( $\chi^2$ ) were controlled below  $0.1$ . The average valence state of manganese ( $V_{\text{Mn}}$ ) was calculated to the equation<sup>40</sup>:

$$V_{\text{Mn}} = 9.69 - 1.27\Delta E_{3s}/\text{eV} \quad (1)$$

Where  $V_{\text{Mn}}$  is the average valence state of manganese,  $\Delta E_{3s}$  is the measured Mn 3s level splitting.

**Electrochemical characterization.** The electrochemical performance was tested on an electrochemical station (Autolab PGSTAT302N) with a built-in EIS analyzer. The electrodes were pretreated as anodes in sulfuric acid solution ( $0.5 \text{ M H}_2\text{SO}_4$ ) at a current density of  $10 \text{ mA cm}^{-2}$  for  $2 \text{ h}$ . Afterward, the working electrode was a carbon cloth (area:  $0.5 \text{ cm}^2$ ). The carbon electrode was used as the counter electrode. The Ag/AgCl (with saturated KCl) was used as the filling solution) electrode served as the reference electrode. The current density ( $j$ ) versus potential ( $U$ ) curves were obtained with a sweep rate of  $1 \text{ mV s}^{-1}$  from  $1.8 \text{ V}$  to  $1.2 \text{ V}$  (vs. RHE) in  $0.5 \text{ M H}_2\text{SO}_4$ . EIS measurements were conducted in a static solution at an overpotential of  $170 \text{ mV}$  from  $0.1 \text{ Hz}$  to  $100 \text{ kHz}$  with an amplitude of  $10 \text{ mV}$ . The electrocatalyst's  $C_{\text{dl}}$  was measured using cyclic voltammograms in a no Faradaic reaction potential window ( $0.99\text{--}1.09 \text{ V}$  vs. RHE) at scanning rates of  $2, 4, 6, 8$ , and  $10 \text{ mV s}^{-1}$ . At  $1.04 \text{ V}$  vs. RHE, the curve of current density difference  $\Delta j = (j_1 - j_2)/2$  with scanning rate is a straight line, and the slope is  $C_{\text{dl}}$ . The mass activity was calculated based on the straight loadings on the carbon cloth working electrode with an area of  $0.5 \text{ cm}^2$  were  $3.592 \text{ mg}$  for  $\text{Mn}_{7.5}\text{O}_{10}\text{Br}_3$ ,  $3.516 \text{ mg}$  for  $\text{Mn}_3\text{O}_{10}\text{Cl}_3$ , and  $3.056 \text{ mg}$  for  $\gamma\text{-MnO}_2$ . All experiments were carried out at ambient temperature ( $25 \pm 2^\circ\text{C}$ ), and the electrode potential was converted to the RHE scale according to given equation:

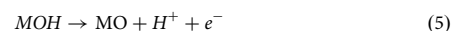
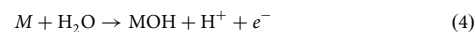
$$E(\text{RHE}) = E(\text{Ag}/\text{AgCl}) + 0.197\text{V} + 0.059\text{pH} \quad (2)$$

**IR correction.** Ohmic loss correction was carried out for polarization curves on different support surfaces. The correction was done according to the given equation<sup>54</sup>:

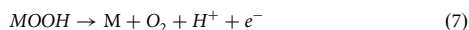
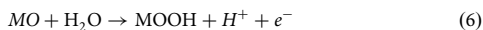
$$E_{\text{corrected}} = E - iR \quad (3)$$

Where  $E_{\text{corrected}}$  is the potential corrected by IR,  $E$  is the potential measured in experiment, and  $R$  is the series resistance measured.

### Acid OER pathway







**TOF calculations of Mn<sub>7.5</sub>O<sub>10</sub>Br<sub>3</sub>, Mn<sub>8</sub>O<sub>10</sub>Cl<sub>3</sub>, and γ-MnO<sub>2</sub> in this work.** The TOFs of these catalysts were calculated using the following equation<sup>55</sup>:

$$TOF = \frac{J * A * \eta}{4 * F * n} \quad (8)$$

*J* is obtained at iR-corrected overpotential = 300 mV, normalized by the geometric area of carbon cloth (0.5 cm<sup>2</sup>); *R* is the series resistance obtained from EIS fitting. *A* is the geometric area of carbon cloth (0.5 cm<sup>2</sup>). *F* is the Faraday constant, and *η* is the Faradaic efficiency. *n* is the mole number of loading manganese atoms on the electrode.

**Faradaic efficiency of oxygen.** Online gas chromatography (Trace GC Ultra, Thermo Scientific) was used to test the Faraday efficiency of oxygen. The details of the instrument have been shown in previous work<sup>56</sup>. The gas chromatography was calibrated by injecting a known concentration of oxygen gas dissolved in the Helium matrix (99.9999%). The peak area was plotted against the concentration (in ppm) of oxygen, resulting in a linear fitting curve, which was used for quantifying the amount of oxygen during the reaction on three samples (Supplementary Fig. 13).

During the electrolysis process, 99.9999% Helium is used as an inert gas, and the evolved oxygen gas was continuously discharged into the sample circuit at a constant rate of 20 sccm. Three samples were tested for oxygen evolution at 10 mA cm<sup>-2</sup> for 100 min. The average Faraday efficiency is calculated for 7–8 injections during electrolysis (except for the first injection, which takes about 20 min to equilibrate the headspace).

The Faradaic efficiency is calculated as follows:

$$\text{Faradaic efficiency (\%)} = \frac{Q}{Q_o} \times 100\% \quad (9)$$

*Q* represents the charge for producing oxygen

*Q<sub>o</sub>* represents charge used for electrolysis

Each injection represents the amount of oxygen produced during a time period of *t<sub>o</sub>*,

$$t_o = \frac{V}{v} \quad (10)$$

*V* represents the volume of a sample loop

*v* represents the flow rate

The total charge used for electrolysis (*Q<sub>o</sub>*) is calculated as

$$Q_o = \int_t^{t+t_o} I \times dt = I_o \times t_o = I_o \times \frac{V}{v} \quad (11)$$

*I<sub>o</sub>* represents average current during injection

The number of moles oxygen (*n<sub>o</sub>*) for each sampling is calculated as:

$$n_o = \frac{P \times V(\%) \times V}{R \times T} \quad (12)$$

*V<sub>o</sub>*(%) represents the volumetric concentration of the gas, which is determined by the peak area of the oxygen peak and the calibration curve

*T* represents the temperature of the test (*T* = 293 K)

*P* represents the pressure during the test (*P* = 1.01 × 10<sup>5</sup> Pa)

*R* represents the ideal gas constant (*R* = 8.3145 J mol<sup>-1</sup> K<sup>-1</sup>)

The charge used for producing oxygen (*Q*) is calculated as:

$$Q = n_o \times N \times F = \frac{P \times V(\%) \times V}{R \times T} \times N \times F \quad (13)$$

*N* represents the number of electrons/holes passed for one oxygen molecule (*N* = 4)

*F* represents the Faraday constant (*F* = 96485.3 C mol<sup>-1</sup>)

Combining Eqs. (9), (11), and (13), the Faradaic efficiency is calculated as:

$$\text{Faradaic efficiency (\%)} = \frac{\frac{P \times V(\%) \times V}{R \times T} \times N \times F}{I_o \times \frac{V}{v}} \times 100\% = \frac{P \times V(\%) \times N F v}{R \times T \times I_o} \times 100\% \quad (14)$$

**Raman shift calculation of isotope lab.** The Raman shift in 0.5 M H<sub>2</sub>SO<sub>4</sub> (H<sub>2</sub><sup>18</sup>O) of Mn<sub>7.5</sub>O<sub>10</sub>Br<sub>3</sub> catalyst was calculated using the following equation<sup>57</sup>:

The Raman characteristic peak after the exchange of one <sup>18</sup>O atom is σ<sub>1</sub>

$$\sigma_1 = \frac{\vartheta(18_{O-OH})}{\vartheta(16_{O-OH})} = \frac{\sqrt{\frac{m_{18O} + m_{16OH}}{m_{18O} \times m_{16OH}}}}{\sqrt{\frac{m_{16O} + m_{16OH}}{m_{16O} \times m_{16OH}}}} \sigma = 0.9843\sigma \quad (15)$$

The Raman characteristic peak after the exchange of two <sup>18</sup>O atom is σ<sub>2</sub>

$$\sigma_2 = \frac{\vartheta(18_{O-18_{OH}})}{\vartheta(16_{O-16_{OH}})} = \frac{\sqrt{\frac{m_{18O} + m_{18OH}}{m_{18O} \times m_{18OH}}}}{\sqrt{\frac{m_{18O} + m_{16O}}{m_{18O} \times m_{16O}}}} \sigma = 0.9573\sigma \quad (16)$$

**Proton exchange membrane (PEM) electrolyzer.** Membrane electrode assemblies (MEAs) were prepared using a Nafion<sup>®</sup>117 polymer membrane (DuPont, thickness 177.8 μm, N117). Before MEAs preparation, the N117 membrane was boiled separately for half an hour in the following solutions to remove possible contaminants and ensure complete protonation: first 3 wt.% H<sub>2</sub>O<sub>2</sub>, then Milliq ultra-pure water, then 1.0 M H<sub>2</sub>SO<sub>4</sub>, and finally Milliq ultra-pure water. Finally, the N117 film is dried in a 40 °C oven for several hours before use. The MEAs were prepared using Pt as the cathode for the hydrogen evolution reaction and Mn<sub>7.5</sub>O<sub>10</sub>Br<sub>3</sub> as the anode for the oxygen evolution reaction. The OER catalyst of Mn<sub>7.5</sub>O<sub>10</sub>Br<sub>3</sub> was directly synthesized on carbon paper (TGP-H-060 purchased from Adrian Electronic Technology Co., LTD). The Pt/c (20 wt% Pt on carbon black purchased from innochem) deposited onto carbon paper was used as the HER catalyst. The mass loadings were controlled at 3.2 mg ± 0.5 cm<sup>-2</sup> of Mn<sub>7.5</sub>O<sub>10</sub>Br<sub>3</sub> and 0.2 mg cm<sup>-2</sup> of Pt for anodic and cathodic catalysts, respectively. The effective area of the MEA was 2 cm × 2 cm (4 cm<sup>2</sup>). Electrolysis tests were conducted using a single cell PEM electrolyzer. The titanium meshes were used as gas diffusion layers for both the anode and cathode. During the test, the cell was maintained at 50 °C, and the pre-heated DI water was fed to the anode at a flow rate of 10 ml min<sup>-1</sup> (pipe diameter 4.8 mm).

**DFT calculations.** Spin-polarized DFT + U calculations were performed using the VASP code<sup>58</sup> with the *U<sub>eff</sub>* value of 3.9 eV for Mn 3d, which is in line with the Materials Project<sup>33</sup>. Electronic exchange and correlations were described by the generalized gradient approximation method with the revised Perdew–Burke–Ernzerhof functional<sup>52</sup>. Core electrons were described by the projector augmented wave method. Valence electrons were described by expanding the Kohn–Sham wave functions in a plane-wave basis set. The energy cutoff for all of the calculations was set as 400 eV. Convergence was defined when all the forces of each atom were below 0.05 eV per Å. (3 × 3 × 1) k-point meshes were used to sample the Brillouin zone using the Gamma point sampling. The bulk Pourbaix diagram was calculated using the Strongly Constrained and Appropriately Normed (SCAN) functional<sup>59</sup>, which has been recently shown to accurately predict the aqueous stability of solids<sup>24</sup>. The detailed construction of Pourbaix diagram was provided in Ref. 60<sup>60</sup> and Ref. 24. In SCAN calculations, the plane wave energy cutoff was 520 eV. The electronic energy and structure relaxation were converged to 10<sup>-5</sup> eV and 0.02 eV/Å, respectively. The Brillouin zone was integrated with a k-point density of 1000 per reciprocal atom. The microkinetic OER activity model was developed based on the methods and scaling relations described in Ref. 50.

## Data availability

All data necessary to support the findings of this study are available in the Supplementary Information. The raw data are available from the corresponding author upon reasonable request. Source data are provided in this paper.

Received: 8 September 2021; Accepted: 14 April 2022;

Published online: 28 April 2022

## References

- An, L. et al. Recent development of oxygen evolution electrocatalysts in acidic environment. *Adv. Mater.* **33**, 2006328 (2021).
- Carmo, M., Fritz, D. L., Merge, J. & Stolten, D. A comprehensive review on PEM water electrolysis. *Int. J. Hydrog. Energy* **38**, 4901–4934 (2013).
- Fujii, K. et al. Characteristics of hydrogen generation from water splitting by polymer electrolyte electrochemical cell directly connected with concentrated photovoltaic cell. *Int. J. Hydrog. Energy* **38**, 14424–14432 (2013).
- Ursua, A., Gandia, L. M. & Sanchis, P. Hydrogen production from water electrolysis: current status and future trends. *Proc. Ieee* **100**, 410–426 (2012).
- Balamurugan, J., Nguyen, T. T., Aravindan, V., Kim, N. H. & Lee, J. H. Highly reversible water splitting cell building from hierarchical 3D nickel manganese oxyphosphide nanosheets. *Nano Energy* **69**, 104432 (2020).
- Roger, I., Shipman, M. A. & Symes, M. D. Earth-abundant catalysts for electrochemical and photoelectrochemical water splitting. *Nat. Rev. Chem.* **1**, 1–13 (2017).
- Spori, C., Kwan, J. T. H., Bonakdarpour, A., Wilkinson, D. P. & Strasser, P. The stability challenges of oxygen-evolving catalysts: towards a common



- fundamental understanding and mitigation of catalyst degradation. *Angew. Chem. Int. Ed.* **56**, 5994–6021 (2017).
8. Lin, Y. C. et al. Chromium-ruthenium oxide solid solution electrocatalyst for highly efficient oxygen evolution reaction in acidic media. *Nat. Commun.* **10**, 1–13162 (2019).
  9. Diaz-Morales, O. et al. Iridium-based double perovskites for efficient water oxidation in acid media. *Nat. Commun.* **7**, 1–612363 (2016).
  10. Lv, H. et al. Ultrathin PdPt bimetallic nanowires with enhanced electrocatalytic performance for hydrogen evolution reaction. *Appl. Catal. B-Environ.* **258**, 525–532 (2018).
  11. Sun, Y. et al. Ultrathin PtPd-based nanorings with abundant step atoms enhance oxygen catalysis. *Mater. Mater.* **30**, 1802136 (2018).
  12. Sun, Y. et al. Covalency competition dominates the water oxidation structure-activity relationship on spinel oxides. *Nat. Catal.* **2**, 736–772 (2020).
  13. Moysiadiou, A., Lee, S., Hsu, C.-S., Chen, H. M. & Hu, X. Mechanism of oxygen evolution catalyzed by cobalt oxyhydroxide: cobalt superoxide species as a key intermediate and dioxygen release as a rate-determining step. *J. Am. Chem. Soc.* **142**, 11901–11914 (2020).
  14. Tao, H. B. et al. Revealing energetics of surface oxygen redox from kinetic fingerprint in oxygen electrocatalysis. *J. Am. Chem. Soc.* **141**, 13803–13811 (2019).
  15. Pan, S. et al. Rational modulating electronegativity of substituents in amorphous metal-organic frameworks for water oxidation catalysis. *Int. J. Hydrog. Energy* **45**, 9723–9732 (2020).
  16. Wang, L., Wang, L., Du, Y., Xu, X. & Dou, S. X. Progress and perspectives of bismuth oxyhalides in catalytic applications. *Mater. Today Phys.* **16**, 100294 (2021).
  17. Zhou, L. et al. Rutile alloys in the Mn-Sb-O system stabilize Mn<sup>3+</sup> to enable oxygen evolution in strong acid. *ACS Catal.* **8**, 10938–10948 (2018).
  18. Yang, X. L. et al. Highly acid-durable carbon-coated Co<sub>3</sub>O<sub>4</sub> nanoarrays as efficient oxygen evolution electrocatalysts. *Nano Energy* **25**, 42–50 (2016).
  19. Mondschein, J. S. et al. Intermetallic Ni<sub>2</sub>Ta electrocatalyst for the oxygen evolution reaction in highly acidic electrolytes. *Inorg. Chem.* **57**, 6010–6015 (2018).
  20. Yao, Y. et al. Engineering the electronic structure of single atom Ru sites via compressive strain boosts acidic water oxidation electrocatalysis. *Nat. Catal.* **2**, 304–313 (2019).
  21. Chatti, M. et al. Intrinsically stable in situ generated electrocatalyst for long-term oxidation of acidic water at up to 80 degrees C. *Nat. Catal.* **2**, 457–465 (2019).
  22. Blasco-Ahicart, M., Soriano-Lopez, J., Carbo, J. J., Poblet, J. M. & Galan-Mascaros, J. R. Polyoxometalate electrocatalysts based on earth-abundant metals for efficient water oxidation in acidic media. *Nat. Chem.* **10**, 24–30 (2018).
  23. Li, A. et al. Stable potential windows for long-term electrocatalysis by manganese oxides under acidic conditions. *Angew. Chem. Int. Ed.* **58**, 5054–5058 (2019).
  24. Wang, Z., Guo, X., Montoya, J. & Nørskov, J. K. Predicting aqueous stability of solid with computed Pourbaix diagram using SCAN functional. *npj Comput. Mater.* **6**, 1–7 (2020).
  25. Frydendal, R., Paoli, E. A., Chorkendorff, I., Rossmeisl, J. & Stephens, I. E. L. Toward an active and stable catalyst for oxygen evolution in acidic media: Ti-stabilized MnO<sub>2</sub>. *Adv. Energy Mater.* **5**, 1500991 (2015).
  26. Kang, Q. et al. Effect of interlayer spacing on the activity of layered manganese oxide bilayer catalysts for the oxygen evolution reaction. *J. Am. Chem. Soc.* **139**, 1863–1870 (2017).
  27. Cho, K. H. et al. Uniform, assembled 4 nm Mn<sub>3</sub>O<sub>4</sub> nanoparticles as efficient water oxidation electrocatalysts at neutral pH. *Adv. Funct. Mater.* **30**, 1910424 (2020).
  28. Ye, Z., Li, T., Ma, G., Dong, Y. & Zhou, X. Metal-ion (Fe, V, Co, and Ni)-doped MnO<sub>2</sub> ultrathin nanosheets supported on carbon fiber paper for the oxygen evolution reaction. *Adv. Funct. Mater.* **27**, 1704083 (2017).
  29. Lkone, P., Euzen, P., Palvadeau, P. & Rouxe, J. Investigations by magnetic measurements and neutron diffraction studies of the magnetic ordering of Mn<sub>8</sub>O<sub>10</sub>Cl<sub>3</sub>. *J. Magn. Magn. Mater.* **12**, 153–164 (1997).
  30. Euzen, P. et al. Synthesis and structural studies of manganese oxyhalides with a multisite framework: part two: Mn<sub>7.5</sub>O<sub>10</sub>Br<sub>3</sub>, a new lacunar oxybromide. *Mater. Res. Bull.* **27**, 1295–1300 (1992).
  31. Euzen, P. et al. Synthesis and structural studies of manganese oxyhalides with a multisite framework: part two: Mn<sub>7.5</sub>O<sub>10</sub>Br<sub>3</sub>, a new lacunar oxybromide. *Mater. Res. Bull.* **27**, 1423–1430 (1992).
  32. Seitz, L. C. et al. A highly active and stable IrO<sub>2</sub>/SrIrO<sub>3</sub> catalyst for the oxygen evolution reaction. *Science* **353**, 1011–1014 (2016).
  33. Jain, A. et al. Commentary: The Materials Project: a materials genome approach to accelerating materials innovation. *APL Mater.* **1**, 011002 (2013).
  34. Su, J. et al. Assembling ultrasmall copper-doped ruthenium oxide nanocrystals into hollow porous polyhedra: Highly robust electrocatalysts for oxygen evolution in acidic media. *Adv. Mater.* **30**, 1801351 (2018).
  35. Surendranath, Y., Kanan, M. W. & Nocera, D. G. Mechanistic studies of the oxygen evolution reaction by a cobalt-phosphate catalyst at neutral pH. *J. Am. Chem. Soc.* **132**, 16501–16509 (2010).
  36. Guan, J. et al. Synthesis and demonstration of subnanometric iridium oxide as highly efficient and robust water oxidation catalyst. *ACS Catal.* **7**, 5983–5986 (2017).
  37. Song, F. & Hu, X. Exfoliation of layered double hydroxides for enhanced oxygen evolution catalysis. *Nat. Commun.* **5**, 1–9 (2014).
  38. Ye, S., Ding, C. & Li, C. Artificial photosynthesis systems for catalytic water oxidation. *Adv. Inorg. Chem.* **74**, 0898–8838 (2019).
  39. Biesinger, M. C. et al. Resolving surface chemical states in XPS analysis of first row transition metals, oxides and hydroxides: Cr, Mn, Fe, Co and Ni. *Appl. Surf. Sci.* **257**, 2717–2730 (2011).
  40. Beyreuther, E., Grafstrom, S., Eng, L. M., Thiele, C. & Dorr, K. XPS investigation of Mn valence in lanthanum manganese thin films under variation of oxygen content. *Phys. Rev. B* **73**, 155425 (2006).
  41. Julien, C. Raman spectra of birnessite manganese dioxides. *Solid State Ion.* **159**, 345–356 (2003).
  42. Julien, C. M., Massot, M. & Poincignon, C. Lattice vibrations of manganese oxides. *Spectrochim. Acta Part A: Mol. Biomol. Spectrosc.* **60**, 689–700 (2004).
  43. Julien, C., Massot, M., Rangan, S., Lemal, M. & Guyomard, D. Study of structural defects in γ-MnO<sub>2</sub> by Raman spectroscopy. *J. Raman Spectrosc.* **33**, 223–228 (2002).
  44. Pitarch, A. et al. In situ characterization by Raman and X-ray fluorescence spectroscopy of post-Paleolithic blackish pictographs exposed to the open air in Los Chaparros shelter (Albalate del Arzobispo, Teruel, Spain). *Anal. Methods* **6**, 6641–6650 (2014).
  45. Wang, L., Duan, G., Chen, S.-M. & Liu, X. Hydrothermally controlled synthesis of alpha-MnO<sub>2</sub>, gamma-MnOOH, and Mn<sub>3</sub>O<sub>4</sub> nanomaterials with enhanced electrochemical properties. *J. Alloy. Compd.* **752**, 123–132 (2018).
  46. Gosztola, D. & Weaver, M. J. Electroinduced structural changes in manganese dioxide+ manganese hydroxide films as characterized by real-time surface-enhanced Raman spectroscopy. *J. Electroanal. Chem. Interfacial Electrochem.* **271**, 141–154 (1989).
  47. Kiefer, C. E. A. W. Raman spectra of the permanganate ion in the solid state with excitation in the near infrared. *J. Raman Spectrosc.* **22**, 715–719 (1991).
  48. Kiefer, W. & Bernstein, H. J. Resonance Raman effect in MnO<sub>4</sub><sup>−</sup> with 5145 Å laser excitation. *Chem. Phys. Lett.* **8**, 381–383 (1971).
  49. Singh, A. K. et al. Electrochemical stability of metastable materials. *Chem. Mater.* **29**, 10159–10167 (2017).
  50. Dickens, C. F., Kirk, C. & Nørskov, J. K. Insights into the electrochemical oxygen evolution reaction with ab initio calculations and microkinetic modeling: beyond the limiting potential volcano. *J. Phys. Chem. C* **123**, 18960–18977 (2019).
  51. Henkelman, G., Uberuaga, B. P. & Harnes, J. A climbing image nudged elastic band method for finding saddle points and minimum energy paths. *J. Chem. Phys.* **113**, 9901–9904 (2000).
  52. Hammer, B., Hansen, L. B. & Nørskov, J. K. Improved adsorption energetics within density-functional theory using revised\_Perdew-Burke-Ernzerhof functionals. *Phys. Rev. B* **59**, 7413 (1999).
  53. Ravel, B. & Newville, M. ATHENA, ARTEMIS, HEPHAESTUS: data analysis for X-ray absorption spectroscopy using IFFFIT. *J. Synchrotron. Radiat.* **12**, 537–541 (2005).
  54. Pan, S. et al. An over 20% solar-to-hydrogen efficiency system comprising a self-reconstructed NiCoFe-based hydroxide nanosheet electrocatalyst and monolithic perovskite/silicon tandem solar cell. *J. Mater. Chem. A* **9**, 14085–14092 (2021).
  55. Bo, Z. et al. Homogeneously dispersed, multimetal oxygen-evolving catalysts. *Science* **352**, 333–337 (2016).
  56. Asiri, A. M. et al. Solid-state synthesis of CdFe<sub>2</sub>O<sub>4</sub> binary catalyst for potential application in renewable hydrogen fuel generation. *Sci. Rep.* **12**, 1–10 (2022).
  57. Fukata, N. et al. Formation of hydrogen-boron complexes in boron-doped silicon treated with a high concentration of hydrogen atoms. *Phys. Rev. B* **72**, 245209 (2005).
  58. Kresse, G. & Furthmüller, J. Efficient iterative schemes for ab initio total-energy calculations using a plane-wave basis set. *Phys. Rev. B* **54**, 11169 (1996).
  59. Sun, J., Ruzsinszky, A. & Perdew, J. P. Strongly constrained and appropriately normed semilocal density functional. *Phys. Rev. Lett.* **115**, 036402 (2015).
  60. Persson, K. A., Waldwick, B., Lazic, P. & Ceder, G. Prediction of solid-aqueous equilibria: Scheme to combine first-principles calculations of solids with experimental aqueous states. *Phys. Rev. B* **85**, 235438 (2012).

## Acknowledgements

The authors gratefully acknowledge the supports from International Cooperation Project of the Ministry of Science and Technology (2014DFE60170), the National Natural Science Foundation of China (Grant No. 61674084), the Overseas Expertise Introduction Project for Discipline Innovation of Higher Education of China (Grant No. B16027), Tianjin Science and Technology Project (Grant No. 18ZXJMTG00220), Financial

support was provided by the Haihe Laboratory of Sustainable Chemical Transformations, and the Fundamental Research Funds for the Central Universities, Nankai University (Grant No. 63211108). D.L. gratefully acknowledged Natural Science Basic Research Program of Shaanxi (program no. 2020JQ-136) and “the Fundamental Research Funds for the Central Universities” (G2020KY0519). J.L. acknowledged funding from the European Union’s Horizon 2020 Research and Innovation program under the Marie Skłodowska-Curie Grant Agreement No. 838686. B.Z. and R.H. acknowledged funding from NSFC (21875042) and STCSM (21DZ1207102, and 21DZ1207103). The authors also thank Jens K. Nørskov for the helpful discussion on the theoretical calculations.

### Author contributions

X.Z. and S.P. proposed the research and designed the experiments. S.P. carried out the experiments. H.L. and Z.W. conducted DFT calculations and analyzed the data. X.P. and R.H. performed In-situ Raman characterizations. D.R. performed Faradaic efficiency of oxygen and helped with the analysis. J.L. and M.S. performed the XAFS test and analysis. S.P., H.L., and Z.W. wrote the manuscript. D.L., Q.Z., M.W., C.W., B.Z., Y.Z., and L.M. helped the analysis. Z.W., M.G., and X.Z. improved the manuscript and contributed to the electrochemical analysis. All authors read and commented on the manuscript. X.Z. directed the overall project.

### Competing interests

The authors declare no competing interests.

### Additional information

**Supplementary information** The online version contains supplementary material available at <https://doi.org/10.1038/s41467-022-30064-6>.

**Correspondence** and requests for materials should be addressed to Zhenbin Wang, Michael Graetzel or Xiaodan Zhang.

**Peer review information** *Nature Communications* thanks Joel Brock and the other, anonymous, reviewer(s) for their contribution to the peer review of this work.

**Reprints and permission information** is available at <http://www.nature.com/reprints>

**Publisher’s note** Springer Nature remains neutral with regard to jurisdictional claims in published maps and institutional affiliations.



**Open Access** This article is licensed under a Creative Commons Attribution 4.0 International License, which permits use, sharing, adaptation, distribution and reproduction in any medium or format, as long as you give appropriate credit to the original author(s) and the source, provide a link to the Creative Commons license, and indicate if changes were made. The images or other third party material in this article are included in the article’s Creative Commons license, unless indicated otherwise in a credit line to the material. If material is not included in the article’s Creative Commons license and your intended use is not permitted by statutory regulation or exceeds the permitted use, you will need to obtain permission directly from the copyright holder. To view a copy of this license, visit <http://creativecommons.org/licenses/by/4.0/>.

© The Author(s) 2022